minerals

MDPI

Article

Facies and Carbon Isotope Variations during the Kungurian (Early Permian) in the Chihsia Formation in the Lower Yangtze Region of South China

Chaogang Fang [1,2,3], Chengcheng Zhang [1,4,*], Xiao Bai [1], Hailei Tang [2], Jiangqin Chao [2] and Hengye Wei [5,6,*]

1 Nanjing Center, China Geological Survey, Nanjing 210016, China
2 Institute of International Rivers and Eco-Security, Yunnan University, Kunming 650500, China
3 Hubei Key Laboratory of Paleontology and Geological Environment Evolution, Wuhan 430205, China
4 Exploration Research Institute, Anhui Provincial Bureau of Coal Geology, Hefei 230088, China
5 School of Geoscience and Technology, Southwest Petroleum University, Chengdu 610500, China
6 Qiangtang Institute of Sedimentary Basin, Southwest Petroleum University, Chengdu 610500, China
* Correspondence: zhangcc3614@foxmail.com (C.Z.); weihengye@163.com (H.W.)

Abstract: The Kungurian Stage in the early Permian was a transitional glacial age between the late Paleozoic icehouse and the early Mesozoic super-greenhouse period This stage offers an excellent opportunity to study the co-evolution between global carbon cycles and environments. This study presents facies and carbon isotope variations in a new carbonate section in the Lower Yangtze region of South China in order to understand the linkage between carbon cycle fluctuation, sedimentary environment, and climate change. Based on the sedimentary facies analyses of the Chihsia Formation (Kungurian), seven facies types were identified and grouped into lower slope, upper slope, and platform facies associations. The facies analyses show that the Kungurian Stage experiences two transgressive-regressive cycles; paleoclimatic changes controlled the sedimentary records and sea level fluctuations. Early Kungurian carbonate rocks record the presence of the short-lived Kungurian carbon isotopic event (KCIE). The rapid negative carbon isotope of the KCIE was closely related to the huge CO_2 emission. A warming climate could have slowed down oceanic ventilation rates and accelerated stratification of seawater. The resulting anoxic environment led to a sharp decline in biological species. In the middle Kungurian, the intensity of volcanic activity gradually weakened and the climate turned cold, which accelerated oceanic ventilation rates and led to increased oxygenation of deep-shelf water masses. The higher $\Delta^{13}C$ values supported enhanced primary productivity and photosynthesis, which promote the prosperity of biological species. This study provides a new perspective for better understanding the links between marine carbon cycle fluctuations, climate change, and environments during the icehouse to greenhouse conversion period.

Keywords: Kungurian Stage; carbon isotope; carbon cycle; climate fluctuation; Lower Yangtze region

check for updates

Citation: Fang, C.; Zhang, C.; Bai, X.; Tang, H.; Chao, J.; Wei, H. Facies and Carbon Isotope Variations during the Kungurian (Early Permian) in the Chihsia Formation in the Lower Yangtze Region of South China. *Minerals* **2023**, *13*, 551. https://doi.org/10.3390/min13040551

Academic Editor: János Haas

Received: 24 February 2023
Revised: 31 March 2023
Accepted: 11 April 2023
Published: 13 April 2023

Copyright: © 2023 by the authors. Licensee MDPI, Basel, Switzerland. This article is an open access article distributed under the terms and conditions of the Creative Commons Attribution (CC BY) license (https://creativecommons.org/licenses/by/4.0/).

1. Introduction

The late Paleozoic ice age, which lasted for nearly 100 million years, is the longest-lived ice age of the Phanerozoic [1–3]. Many studies have been performed on the regulation of changes in sea level [4,5], the terrestrial ecosystem [6,7], fluctuations of the atmospheric CO_2 concentration [8–12], biocrises in the Carboniferous [13,14], and tectonic setting [15] during the Late Paleozoic Ice Age (LPIA), which provide valuable insights into the trigger mechanism of this ice age and its coevolution with the ecosystem. Previous studies had focused mainly on the initial [1,2,16] and terminal [2,17] stages of the LPIA; however, the climate transition from the late Paleozoic icehouse to the early Mesozoic super-greenhouse as well as the corresponding mechanism are rarely explored [18]. The Kungurian of the early Permian is one of the most important stages during this transition, which experienced dramatic disturbances of the global carbon cycle [19–21], such as the significant negative

shifts of carbon isotopes in ~277.9–277.4 Ma (the so-called KCIE event) [19]. Therefore, it is of academic interest to explore the mechanisms of climate transition during and after the LPIA by studying the Kungurian carbon cycle.

At present, there are few studies on the carbon cycle and climate transition mechanisms during the Kungurian Stage in South China. Liu et al. [19,20] reported a case study in the Youjiang Basin in South China based on the restricted environment. In this paper, a platform-slope section of open marine environment in the Lower Yangtze region can offer a more detailed record of the carbon cycling and paleoceanic conditions during the Kungurian in South China. Using a precise stratigraphic framework of conodont zones [22], we study detailed facies variations and carbon isotope composition features during the Kungurian in South China so as to explore the cause for the KCIE and the origin of the glaciation termination.

2. Geological Setting

The Lower Yangtze region in the South China block was situated in the northeast of the Paleo-Tethys ocean system during the Kungurian of the Permian (Figure 1a). The Lower Yangtze region roughly extends in the northeast-southwest direction, close to the paleo-equator. It is adjacent to the Qinling Ocean in the northwest and to the Cathaysia in the southeast [23,24]. Due to the deglaciation in Gondwanaland, the Yangtze area experienced the largest transgression since the late Paleozoic, forming a carbonate platform-slope dominant facies in the Lower Yangtze region [25], which deposited Chihsia limestone [26]. Then, in the Roadian, this area deposits, and accordingly, the water becomes deeper, which is conducive to the sedimentation of black siliceous rocks. The water gets shallower at the end of the sedimentary stage during the Capitanian [27].

Putaoling section (117°46′22.16″ N, 31°32′52.23″ E) is in a new local quarry in the Chaohu area of the Lower Yangtze region. In this outcrop section, the Permian strata are well exposed, including the Chuanshan, Chihsia, and Gufeng Formations in ascending order. According to the regional geological time frame [28], the Kungurian age corresponds to the Chihsia Formation (Figure 1b). This formation is up to 220 m thick and shows a northwestward dip at an angle of 40°~60°, which is favorable for strata observation, description, and sampling. The lithology of the studied Chihsia Formation will be described thoroughly below (Figure 2).

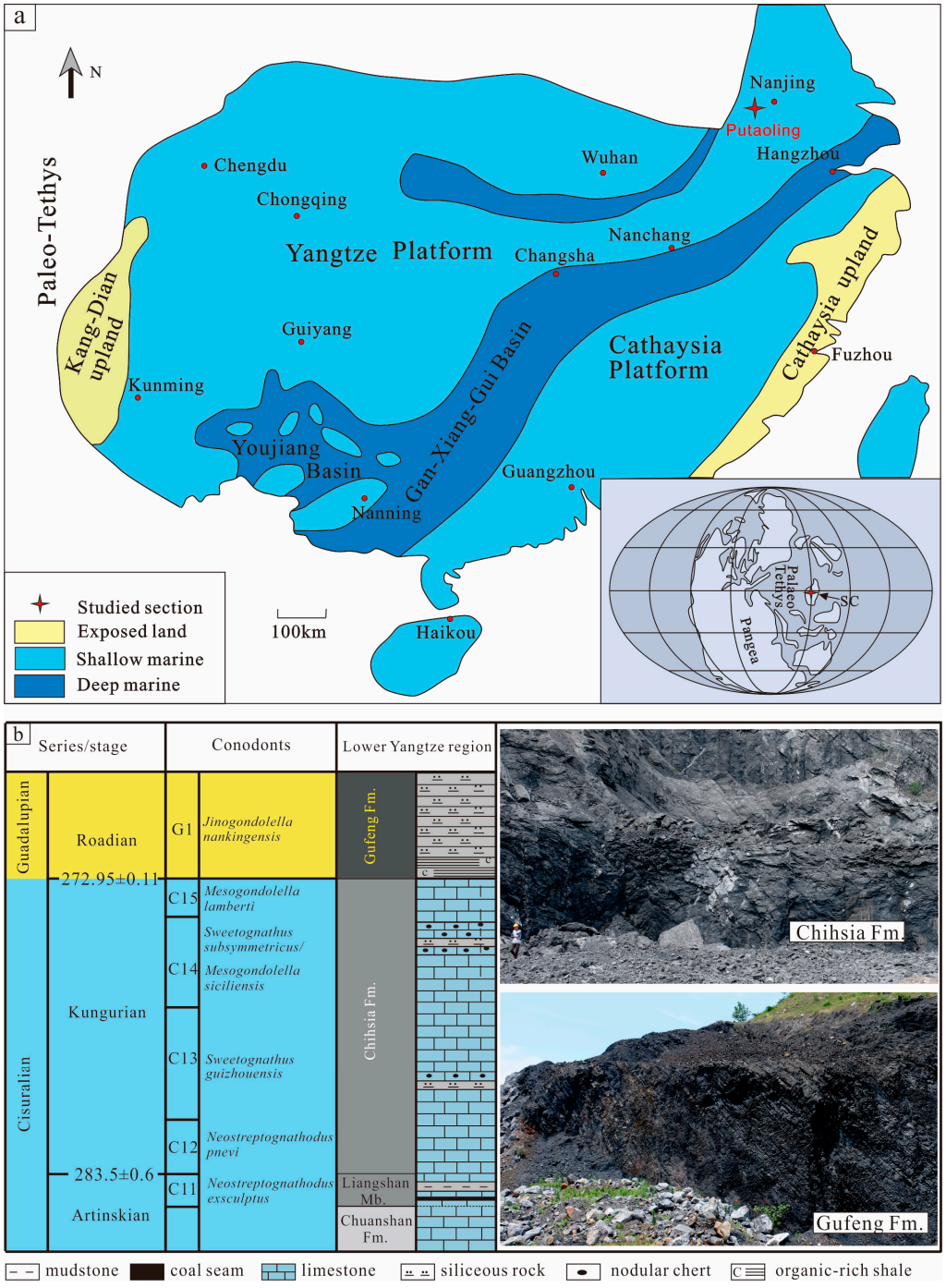


Figure 1. (**a**) Lithofacies palaeogeography during the Kungurian Stage in South China and the location of the studied section (modified from [29]). The inset box shows the global palaeogeography of the early–middle Permian transition. Note the location of the South China block (SC; arrowed) and the studied section (star). (**b**) A stratigraphic framework for the early Permian strata from the Lower Yangtze region (modified from [28]), the general outcrop characteristics of the Chihsia and Gufeng Formations.

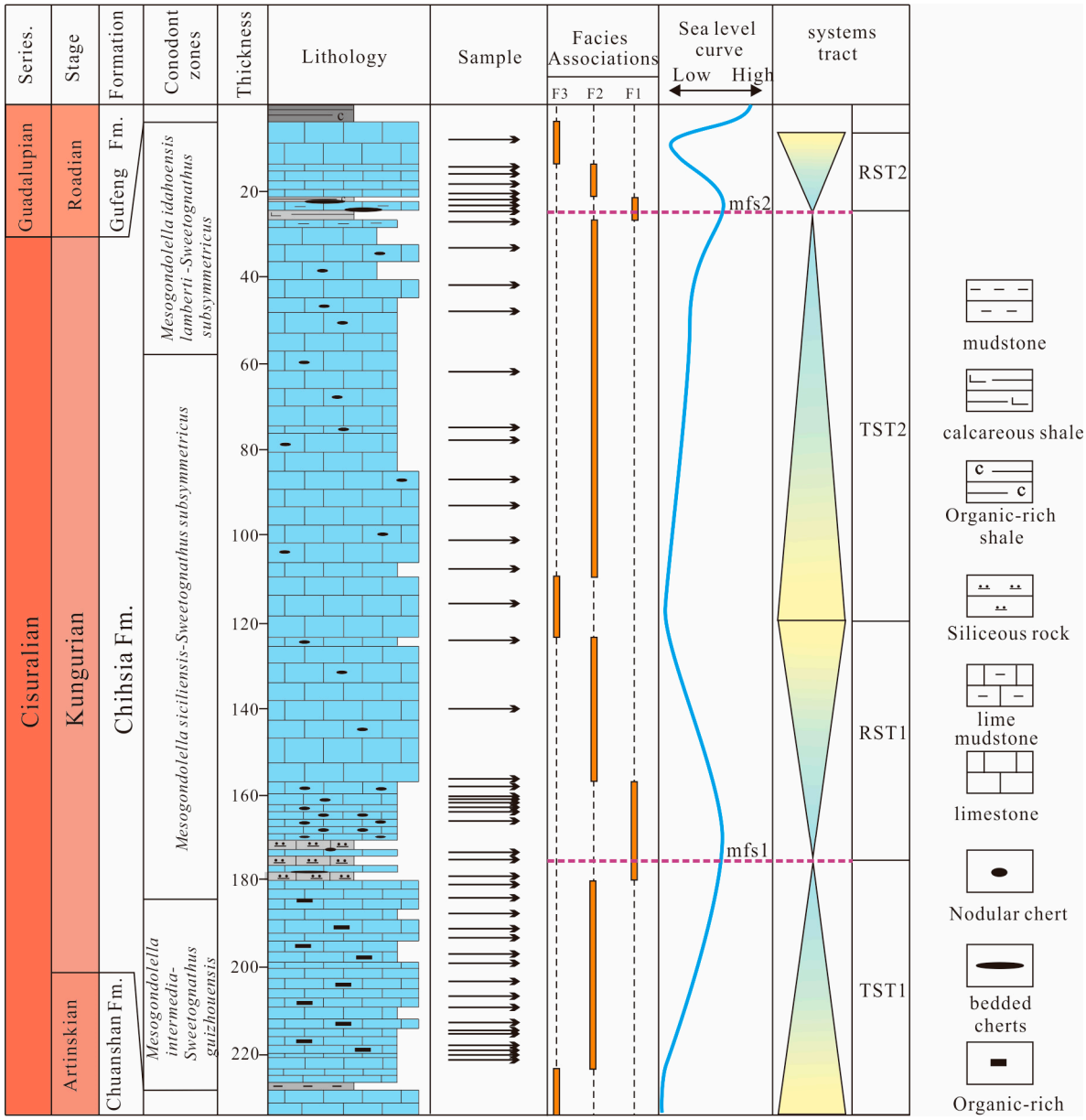


Figure 2. The lithostratigraphy, sedimentary facies, and sampling location at the Putaoling section of Chaohu during the Kungurian (paleontological data modified from [25]). mfs represents the maximum flooding surface.

3. Methods

A total of 50 rock samples (No. T1-T50) of the Chihsia Formation from the Putaoling section were collected for the facies analyses (Figure 2). According to Wilson's facies classification of carbonate [30], facies and facies associations were identified according to lithology, primary sedimentary structure, thickness, color, and fossil assemblage.

The fresh limestone samples were cautiously selected for the isotope analyses, avoiding diagenetic alteration and calcite veins. The thin sections of samples were examined using a microscope and cathode luminescence analysis.

A 100 mg powder sample was added into the centrifuge tube with 4 M HCl solution to digest for 24 h. The residue sample was cleaned in a centrifuge at least three times until the supernatant reached a neutral pH level. Then, the precipitates were frozen and dried in a clean freeze dryer for 36–48 h, thus dissolving and removing the inorganic carbon. Next, 10–15 mg of samples were weighed and wrapped in a tin-weighing boat. After being

compacted and folded, this boat was placed into the LECCO CS230 infrared carbon-sulfur analyzer and measured with a precision of +5%. The above analysis was completed at the Sichuan Keyuan Engineering Technology Testing Center.

For the inorganic-carbon isotope measurement, a proper amount of carbonate powder samples were baked in an oven for 2 h at 105 °C to remove the absorbed water. Then, 0.1 mg of powder samples were added to the sample tube and covered with a lid carrying high-purity helium. Using the acid pump and needle, an excess of 100% phosphoric acid was added into this tube and reacted with samples to generate CO_2. The CO_2 was brought into the EA-MAT253 mass spectrometer by the high-purity helium to test the isotopic composition of C and O. For every five samples, a standard sample was added to compare and test them based on the reference gas. The measurement results were subject to the PDB, denoted by $\delta^{13}C_{V\text{-}PDB}$ and $\delta^{18}O_{V\text{-}PDB}$, which were analyzed at a precision higher than 0.2‰. The above analysis was conducted by the Supervision and Inspection Center for Mineral Resources in East China, Ministry of Land and Resources.

For the organic-carbon isotope measurement, the powder samples were reacted with 6 M hydrochloric acid at room temperature for 24 h. Then, the distilled water was added for high-speed centrifugation to remove the supernatant until the pH value reached 7. After being pretreated by purifying and drying, the samples were wrapped in a clean silver or tin cup and injected using an autosampler. The organic matter contained in these samples reacted rapidly with the O_2 at 960 °C in a reactor, thus generating N_2 and CO_2. Along the helium flow, at a speed of 90 mL/min, the two gases were dewatered by desiccants and separated by chromatographic columns. Then, the gases passed through the quartz capillaries and were analyzed using the EA-MAT253 isotope ratio mass spectrometer. The measurement results of carbon isotopes were subjected to the PDB at a precision higher than 0.2‰. The above analysis was carried out by the Supervision and Inspection Center for Mineral Resources in East China, Ministry of Land and Resources.

4. Results

4.1. Analyses of Facies

4.1.1. Facies and Facies Associations

Detailed analyses of facies were carried out on the sedimentary succession of the Chihsia Formation (Figure 2). Fourteen types of facies are identified and further grouped into three associations, i.e., lower slope, upper slope, and platform margin. The characteristics and interpretations of different facies associations are discussed in the following section.

Lower slope facies association (F1)

Description

The lower slope facies association includes three types of facies (F1a, F1b, and F1c). Facies 1a are composed of dark-gray to black, thin-bedded (3–8 cm thick) siliceous rock interbedded with grey, medium-bedded (15–30 cm thick) limestone (Figure 3A). The siliceous rock mainly consists of microquartz, radiolarian, and sponge spicule (Figure 3B). The grey limestone consists of lime mudstone and wackestone. Generally, biotic fragments are rare in lime mudstone but are relatively abundant (20%–40%) in wackestone, such as foraminifera (Figure 3C) and echinoderms. These facies were mainly observed in the lower part of the Chihsia Formation.

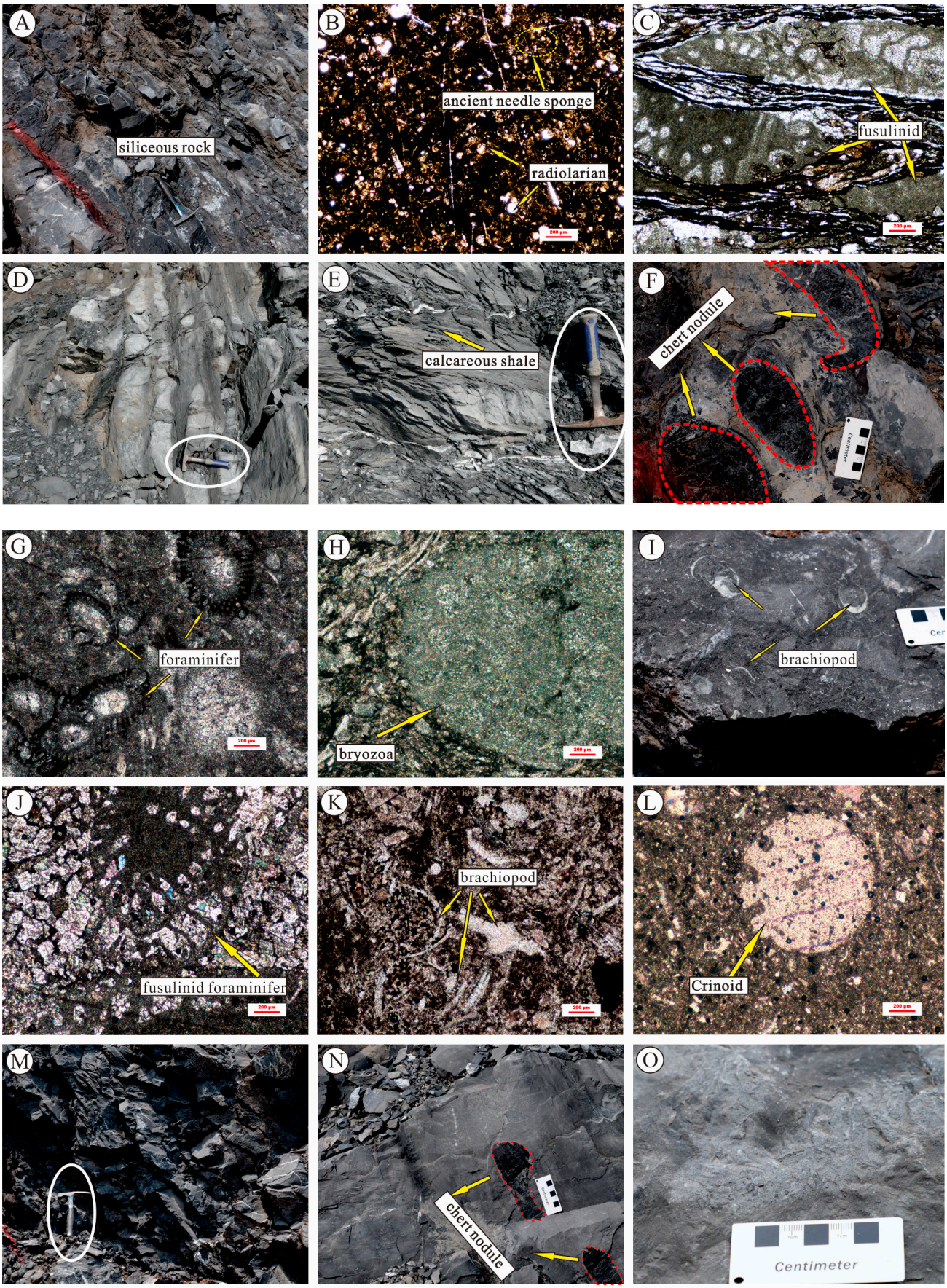


Figure 3. *Cont.*

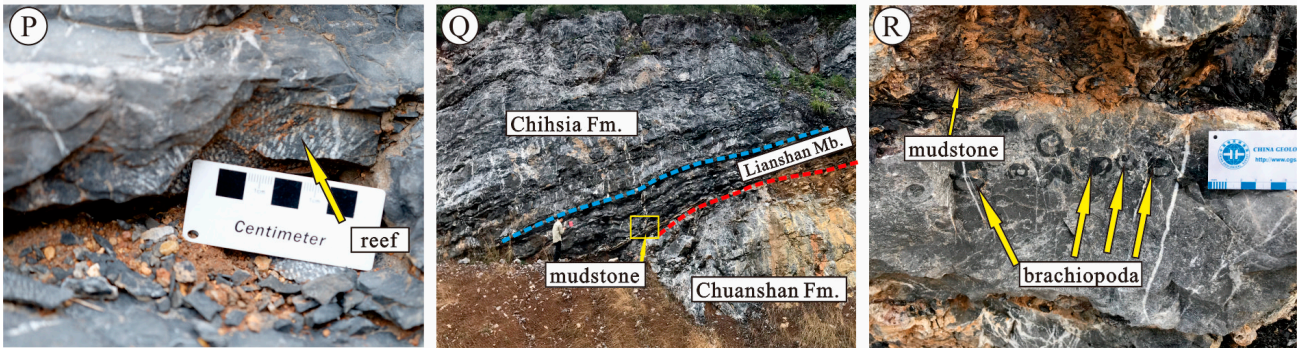


Figure 3. Typical rock types from the Putaoling section collected from the Lower Yangtze region. (**A**) A thin black layer of siliceous rock. (**B**) Siliceous rocks that contain abundant radiolarians and sponge spicules of different sizes. (**C**) Wackestones that contain abundant foraminifera. (**D**) Limestone intercalated with dark grey calcareous shale. (**E**) Calcareous shale. (**F**) Limestone with abundant black lenticular or nodular chert. (**G**) Foraminifera. (**H**) Bryozoan. (**I**) Abundant brachiopods can be seen in the bioclastic limestone. (**J**) Foraminifera. (**K**) Brachiopods. (**L**) Crinoids. (**M**) Medium-bedded wackestone. (**N**) Nodular chert. (**O**) Thick-bedded packstone, abundant bioclasts. (**P**) Corals. (**Q**) Limestone intercalated with a coal seam. (**R**) Abundant brachiopod fossils.

Facies 1b consist of thin- to medium-bedded (5–30 cm thick) limestone intercalated with dark grey calcareous shale (Figure 3D). Similar to that in facies 1a, the limestone in these facies is also composed of lime mudstone and wackestone. In some cases, black, irregular chert nodules were observed in the lime mudstone and presented disorderly. The calcareous shale bed is characterized by thickness ranging from 5 to 8 cm and commonly shows horizontal lamination (Figure 3E).

Facies 1c consist of dark-gray, medium- to thick-bedded (20–80 cm thick) limestone with abundant black lenticular or nodular chert mainly oriented with their long axes approximately parallel to the bed (Figure 3F). Their size ranges between 10 and 20 cm (long axes). Bioclastics in the lime mudstone are rare and mainly consist of foraminifera (Figure 3G), echinoderms, and bryozoans (Figure 3H). These facies usually overlie facies 1a.

Interpretation

The presence of siliceous rock, bedded chert, and horizontal lamination in F2a and F2b suggest a deep-water environment. However, the interbedded limestone mainly contains the shallow-water resedimented fauna, such as foraminifera and bryozoans, which supports that the sedimentation occurs in the lower slope area.

Upper slope facies association (F2)

Description

Two facies (F2a and F2b) are recognized in this facies association. F2a is composed of light gray to gray, medium- to thick-bedded (15–60 cm thick) limestone (Figure 3I). The limestone is predominantly wackestone and packstone. In general, more abundant biotic fragments are present in these facies than in those in the lower slope facies association. The main bioclasts include foraminifera (Figure 3J), brachiopods (Figure 3K), and crinoids (Figure 3L). This facies is very common, and its total thickness reaches approximately 50% of that of the whole Chihsia Formation.

F2b consists of gray, medium-bedded (10–30 cm thick) wackestone (Figure 3M). Occasionally, a small amount of black, irregular nodular chert (Figure 3N) was observed in the wackestone and occurred in a disordered pattern.

Interpretation

Compared to the lower slope facies association, the occurrence of light-gray to gray, thick-bedded wackestone, and packstone with a higher abundance of biotic fragments of shallow-water fauna, as well as lithoclasts, indicates a shallow-water environment. The development of irregular nodular chert further implies an upper slope environment. Noteworthy, this facies association is different from that developed on the Cretaceous

carbonate slope in western Sicily, Italy, reported by Randazzo et al. (2020) [31]. In contrast to the massive breccias with dimensions ranging from pebble size to boulder dimensions caused by debris flows in the Cretaceous carbonate slope, breccias in F2 of this study were rarely observed. This deposition difference is probably associated with their tectonic settings, i.e., tectonically active vs. tectonically stable.

Platform facies association (F3)

Description

There are two facies (F3a) identified in this facies association. F3a comprises light-gray, medium- to thick-bedded (20–60 cm thick) packstone (Figure 3O). Corals (Figure 3P) and sponges, as well as bioclasts of brachiopods and algae, occur in this facies. Compared to the upper slope facies, F3a commonly presents a higher content of bioclasts. Grains in the packstone are locally represented by oncolites, particularly at the bottom of the Chihsia Formation. Their sizes range between 2 and 10 mm, and they are moderately rounded and sorted.

F3b is composed of dark-gray, thin- to medium-bedded (3–12 cm thick) limestone intercalated with black, thin-bedded (2–6 cm thick) mudstone, with a total thickness of around 2 m (Figure 3Q). This facies corresponds to the Liangshan Member, which is an important marker layer and occurs at the bottommost of the Chihsia Formation. The mudstone, characterized by high total organic carbon (TOC) content, was believed to be a low-quality coal seam [32]. Abundant brachiopod fossils were observed in the limestone of this facies (Figure 3R).

Interpretation

The biological types in the facies of F3a and F3b, such as calcareous reefs, sponges, and brachiopod fossils, indicate a shallow-water carbonate platform environment. However, this shallow-water biota could also be observed in slope environments as the result of sediment gravity flows, as reported in some other cases [33,34]. Due to the absence of bottom erosive surfaces (scours), which commonly occur in gravity flow deposits, and the predominant moderate roundness and sorting of grains, we ruled out the possibility of gravity flow deposition. In addition, the existence of the intercalated coal seam, which developed in a littoral system, also supports a shallow water environment.

4.1.2. Transgressive-Regressive (TR) Sequence

The vertical stacking patterns of facies associations are the basis for analyzing transgressive-regressive (TR) sequence [35,36]. A complete TR cycle comprises a transgressive sequence (T) and a regressive sequence (R). A transgressive sequence is characterized by the retrogradation of facies associations as an upward-deepening succession, while a regressive sequence is characterized by the progradation of facies associations as an upward-shallow succession. According to the vertical stacking patterns of the facies association, two TR sequences were identified for the Kungurian strata at Chaohu (Figure 2). The transgressive interval of the two sequences is marked by the platform facies association on the bottom, the upper slope facies association in the center, and the lower slope facies association on the top. Similarly, the regressive interval of the two sequences is marked by lower slope facies association on the bottom, upper slope facies association on the central, and platform facies association on the top.

These two TR sequences are analogous to the two third-order sequences of the Chihsia Formation at Xuanguang of the Lower Yangtze region proposed by [37] and also are basically consistent with the sea-level fluctuations recorded in the Artinskian in North America [38]. Each of these TR sequences was deposited over ~2–4 Myr [39]. Although in this study we cannot precisely quantify the sea level changes during the Kungurian era, we infer a relative sea-level increase during the deposition of the transgressive interval and a relative sea-level decrease during the deposition of the regressive interval.

4.2. Geochemistry

The TOC content ranges between 0.14% and 2.12% in the Putaoling section. It fluctuates rapidly within 0.14%~1.89% in the TST1, presenting a slight rising trend upward, reaching a maximum at the MFS1. TOC values in RST1 and TST2 range from 0.18% to 0.97%, with a mean value of 0.38%. In the next section, it reaches the maximum value of 1.82% at the MSF2 (Table 1 and Figure 4).

Table 1. TOC variations and paired inorganic and organic carbon isotopic data across the Kungurian Marine carbonate rocks from the Putaoling section, Chaohu.

No.	Lithology	TOC/%	$\delta^{13}C_{carb}$/‰	$\delta^{18}O_{carb}$/‰	$\delta^{13}C_{org}$/‰	$^{13}\Delta$/‰
T-1	Limestone	0.41	2.1	−7.6	−27.0	29.1
T-2	Limestone	0.28	1.3	−7.2	−27.6	28.9
T-3	Limestone	1.41	2.1	−7.0	−27.0	29.0
T-4	Limestone	0.30	1.7	−7.0	−27.9	29.7
T-5	Limestone	0.81	1.5	−7.0	−27.8	29.3
T-6	Limestone	1.89	2.2	−7.3	−28.0	30.2
T-7	Limestone	0.26	3.1	−7.4	−27.1	30.2
T-8	Limestone	0.49	2.4	−7.4	−28.0	30.3
T-9	Limestone	0.35	2.5	−6.9	−27.6	30.1
T-10	Limestone	0.44	2.5	−9.3	−27.4	29.9
T-11	Limestone	0.34	2.3	−7.9	−27.8	30.0
T-12	Limestone	0.87	2.7	−7.3	−26.8	29.4
T-13	Limestone	1.26	2.6	−6.6	−27.5	30.1
T-14	Limestone	0.14	2.6	−5.3	−26.6	29.2
T-15	Limestone	0.47	2.9	−5.7	−27.3	30.2
T-16	Limestone	1.51	2.5	−5.5	−27.9	30.4
T-17	Limestone	0.50	2.8	−5.1	−27.3	30.2
T-18	Limestone	1.60	2.1	−5.4	−27.6	29.7
T-19	Limestone	0.39	1.5	−5.5	−28.0	29.5
T-20	Limestone	1.06	1.1	−5.7	−28.2	29.3
T-21	Limestone	0.30	1.9	−6.6	−26.9	28.8
T-22	Limestone	2.12	2.2	−6.9	−27.2	29.4
T-23	Limestone	2.00	2.7	−4.9	−26.5	29.2
T-24	Limestone	0.94	2.2	−6.6	−27.3	29.5
T-25	Limestone	1.26	1.5	−6.5	−27.1	28.6
T-26	Limestone	0.39	1.7	−7.9	−28.6	30.3
T-27	Limestone	1.19	1.7	−8.6	−27.2	28.9
T-28	Limestone	1.68	2.4	−7.7	−27.1	29.5
T-29	Limestone	0.57	3.5	−5.1	−26.8	30.2
T-30	Limestone	0.33	4.3	−5.1	−26.3	30.7
T-31	Limestone	0.34	3.4	−8.5	−27.1	30.6
T-32	Limestone	0.97	3.8	−5.8	−27.3	31.1
T-33	Limestone	0.32	3.6	−5.7	−26.3	29.9
T-34	Limestone	0.23	4.2	−6.1	−24.8	29.0
T-35	Limestone	0.32	4.1	−5.8	−25.8	29.9
T-36	Limestone	0.70	3.1	−6.2	−26.9	30.0
T-37	Limestone	0.27	4.4	−6.1	−26.2	30.5
T-38	Limestone	0.34	4.2	−5.8	−27.2	31.4
T-39	Limestone	0.20	3.8	−5.3	−26.8	30.7
T-40	Limestone	0.29	3.6	−6.9	−26.7	30.3
T-41	Limestone	0.18	3.5	−7.2	−26.2	29.7
T-42	Limestone	0.27	3.1	−6.2	−26.7	29.8
T-43	Calcareous shale	0.61	3.1	−6.2	−27.4	30.6
T-44	Limestone	1.18	2.8	−6.9	−28.3	31.1
T-45	Calcareous shale	1.82	2.8	−6.4	−26.8	29.6
T-46	Limestone	1.57	2.2	−6.4	−27.1	29.3
T-47	Limestone	0.51	2.3	−7.4	−28.0	30.2
T-48	Limestone	0.33	2.7	−6.4	−27.0	29.7
T-49	Limestone	0.65	2.4	−7.1	−27.1	29.5
T-50	Limestone	0.75	2.6	−5.6	−27.3	29.9

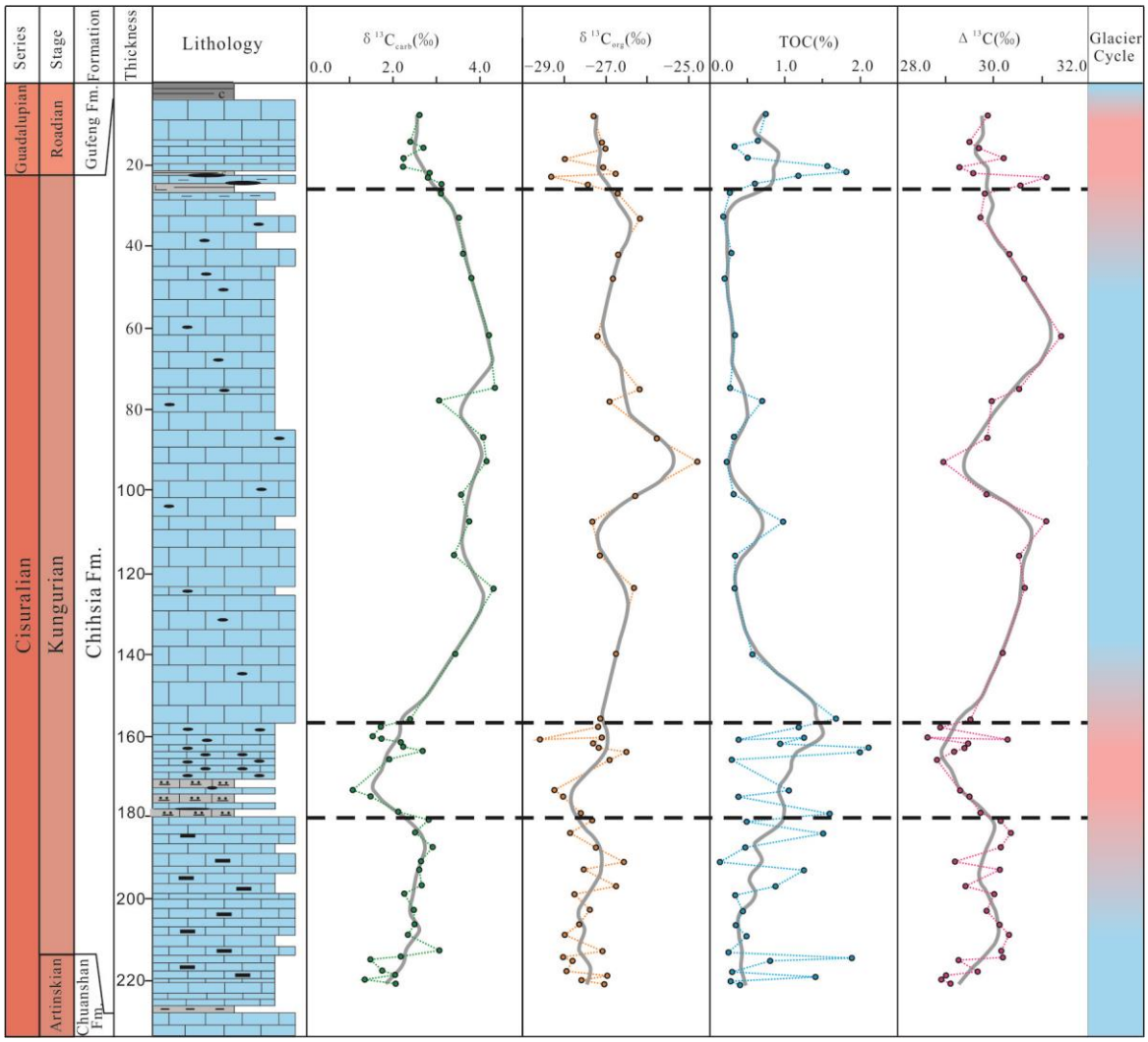


Figure 4. The variation relationship of $^{13}C_{carb}$, $^{13}C_{org}$, TOC, and $\Delta\delta^{13}C$ at the Putaoling section during the Kungurian. The solid curves of the $^{13}C_{carb}$, $^{13}C_{org}$, TOC, and $\Delta\delta^{13}C$ values in the Putaoling section are 3-point running averages.

The $\delta^{13}C_{carb}$ undergoes four stages according to different variation characteristics. It ranges between 1.3‰ and 3.0‰ in TST1 (ascent stage), showing a slight rising trend in the early stage and reaching a stable state in the middle and late stages. In mfs1 nearby (decline stage), $\delta^{13}C_{carb}$ reduces from 2.13‰ to 1.07‰. It is kept within a high-value interval in RST1 and TST2 (stable stage), ranging between 3.1‰ and 4.4‰. In RST2 (slight decline-steady stage), the value stabilizes at 2.3‰~2.7‰ after reducing from 3.1‰ to 2.2‰, showing a small amplitude of fluctuation (Table 1 and Figure 4).

The carbonate $\delta^{13}C_{org}$ values vary between −28.6‰ and −24.8‰ at the Putaoling section. The variation trend of $\delta^{13}C_{org}$ is positively correlated with the $\delta^{13}C_{carb}$ curve, showing a correlation coefficient of 0.5. Similar to $\delta^{13}C_{carb}$, $\delta^{13}C_{org}$ also rises slightly in TST1 but still fluctuates within the range of −28.0‰~−26.6‰. In mfs1 nearby, $\delta^{13}C_{org}$ negatively correlates with $\delta^{13}C_{carb}$ with a similar amplitude of fluctuation (about 1.0‰) of a positive shift. $\delta^{13}C_{org}$ values are higher (−27.3‰~−24.8‰) in RST1 and TST2, and fluctuate in a wider magnitude than the $\delta^{13}C_{carb}$ in the middle stage. In mfs 2 nearby, $\delta^{13}C_{org}$ reduces from −27.4‰ to −28.3‰, and then rises back to about −27.0‰ in RST2, after which $\delta^{13}C_{org}$ changes steadily until it reaches the Gufeng Formation (Table 1 and Figure 4).

$\Delta^{13}C$ changes in a similar way to $\delta^{13}C_{carb}$ at the Putaoling section. It first rises slightly from 28.9 ‰ to 30.4 in TST1. In mfs1 nearby, $\Delta^{13}C$ declines gently to the minimum value of

28.4‰, and its negative shift occurs later than that of $\delta^{13}C_{org}$ and $\delta^{13}C_{carb}$. In RST1 and TST2, $\Delta^{13}C$ increases rapidly from 29.5‰ to 30.2‰, and then reduces to 29.0‰ gradually before rising back to 31.4‰, but at the end of this stage, it declines slowly to 29.5‰ again. $\Delta^{13}C$ fluctuates slightly in RST2, changing within 29.0~31.0‰ (Table 1 and Figure 4).

5. Discussion

5.1. Diagenesis Effects on the Carbon Isotopic Compositions

The carbon and oxygen isotopes in seawater contain a wealth of information regarding paleoclimate and paleoenvironment. However, due to the lack of paleoseawater samples during the reconstruction of the paleo-ocean, these isotopes in the paleo-ocean are indirectly studied based on the characteristics of sediment carriers that are preserved intact, such as carbonate shells and whole rocks. Since these shells are distributed heterogeneously along the profile, a continuous stratigraphic record can be established for the carbon and oxygen isotopes of carbonate [40,41]. According to the microscopic thin section examination, limestones show typical argillaceous microcrystalline texture, which indicates that samples are weakly affected by the diagenesis.

The diagenetic alteration in the isotopic composition of bulk carbonate can also be assessed by means of oxygen isotopic composition. When the $\delta^{18}O$ value is less than −11‰, it means samples have undergone a serious alteration. In this case, the carbon and oxygen isotopes cannot reflect the paleo-ocean information [42]. $\delta^{13}C_{carb}$ and $\delta^{18}O$ tend to decline simultaneously under the influence of diagenesis and consequently present a positive correlation between them [43]. The $\delta^{18}O$ values of −4.9‰ to −9.3‰ and the weak correlation between $\delta^{13}C_{carb}$ and $\delta^{18}O$ ($R^2 = 0.12$), as shown in Figure 5a, suggest a weak diagenetic effect and represent original seawater signals.

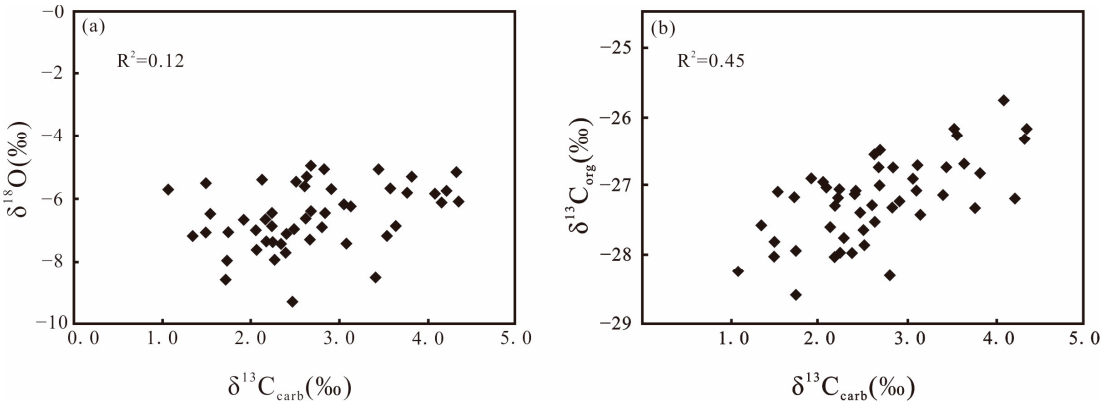


Figure 5. Cross-plots between (**a**) $\delta^{13}C_{carb}$ vs. $\delta^{18}O$ and (**b**) $\delta^{13}C_{carb}$ vs. $\delta^{13}C_{org}$ of the Putaoling section, Chaohu.

The synchronically shifting organic carbon and inorganic carbon isotopic compositions of sediments in this study (Figure 5b) generally reflect environmental information instead of diagenesis [44]. Furthermore, the thermal alteration can only increase the absolute value of $\delta^{13}C_{org}$ but not affect the variation trend [45]. Therefore, the $\delta^{13}C_{org}$ in this study is weakly affected by the thermal alteration and therefore can clearly reflect the paleoseawater information at that time.

5.2. Global Correlation of Kungurian Carbon-Isotope Excursions

The Chihsia Formation in the Putaoling section shows two negative carbon-isotope excursions in the Kungurian, i.e., about a 1.8‰-magnitude excursion in the early Kungurian and about a 0.9‰-magnitude excursion in the later Kungurian (Figure 6). The first negative excursion in the lower Kungurian can be correlated with those in other places such as South China (Guizhou, Tongle, and Guangyuan sections) [19,20,46], North China (Yuzhou coal field) [21], America, Eastern Australia, and South Africa (Figure 6) [47,48]. This global

negative excursion in the early Kungurian is known as the Kungurian carbon isotopic event (KCIE), whose carbon isotopes negative excursion is 1.0‰ to 3.5‰, with an average value of 1.60‰. In the later Kungurian, there is a slight negative shift of $\delta^{13}C$ (0.9‰ in magnitude), which is not a global record of carbon isotope negativity (Figure 6). This may represent a local facies control of carbon isotopic variations. This conclusion is consistent with the facies transition from shallow-water facies to deep-water facies mentioned above.

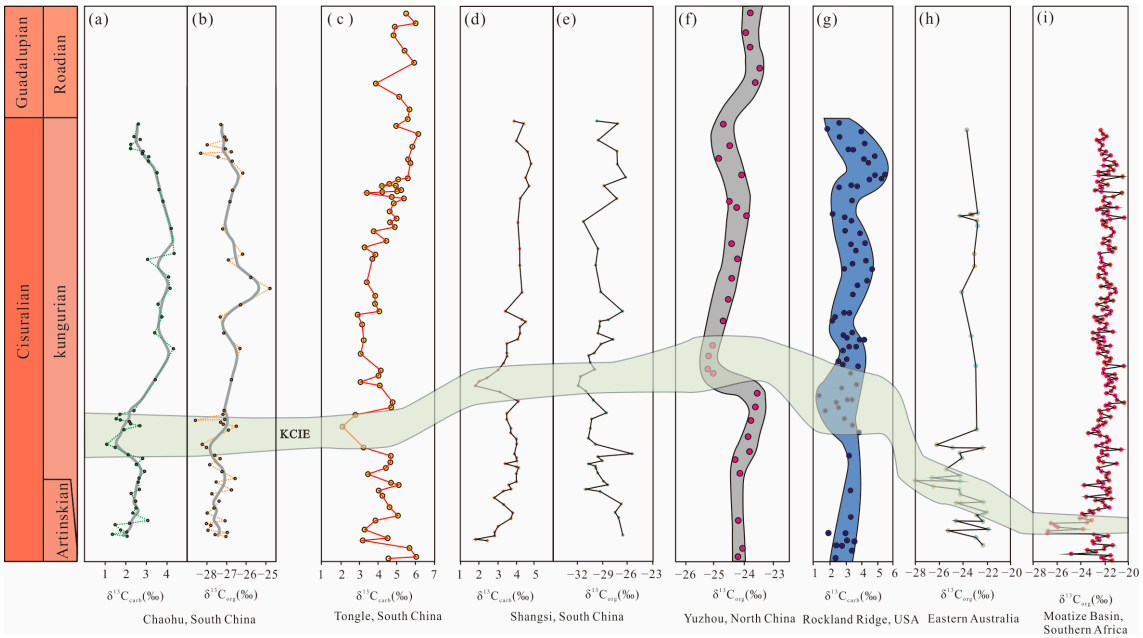


Figure 6. Permian-Kungurian carbon isotope stratigraphic division and correlation. (**a**) $\delta^{13}C_{carb}$ curve in the study area (marine strata, Lower Yangtze region, South China); (**b**) $\delta^{13}C_{org}$ curve in the study area (marine strata, Lower Yangtze region, South China); (**c**) $\delta^{13}C_{carb}$ curve in Tongle section (marine strata, Youjiang Basin, South China; [19]); (**d**) $\delta^{13}C_{carb}$ curve in Shangsi section (marine strata, Sichuan Basin, South China; [46]); (**e**) $\delta^{13}C_{org}$ curve in Shangsi section (marine strata, Sichuan Basin, South China; [46]); (**f**) $\delta^{13}C_{org}$ curve in Yuzhou section (terrestrial strata, North China Platform; [21]); (**g**) $\delta^{13}C_{carb}$ curve in Rockland Ridge section (marine strata, Nevada, USA; [49]); (**h**) $\delta^{13}C_{org}$ curve in Eastern Australia section (terrestrial strata, Australia; [47]); (**i**) $\delta^{13}C_{org}$ curve in Southern Africa section (terrestrial strata, Moatize Basin, Southern Africa; [48]).

5.3. Causes of the KICE during the Early Kungurian

The Permian is an important stage of a drastic climate transition. For example, the extreme icehouse climate in the early Permian (i.e., the peak period of the LPIA) became increasingly warming and entered a long-term greenhouse climate in the late Permian [50]. However, there is still debate about the exact timing of ice melting during the LPIA [51]. Recent research on Permian conodont apatite oxygen isotopes in southern China suggests that the oxygen isotope values decreased from the early-middle Guadalupian and reached their lowest value in the late Kungurian (a 2‰ decrease), indicating that the main ice melting period of the LPIA occurred between the Guadalupian and Kungurian [52]. The depositional period of the Chihsia Formation is the maximum transgression of the Permian in South China, and it just corresponds to Kungurian [53] or includes Kungurian [54]. As such, it is widely believed that the extensive transgression of the Permian in southern China was controlled by this glacial melting event. However, the sea level change does not vary consistently with the variations of the carbon isotope composition in the whole Kungurian. This excludes the rising sea level as the main cause of the KICE.

The KICE coincided with the beginning of the atmosphere's CO_2 rising from 600 $\mu L \cdot L^{-1}$ to 3800 $\mu L \cdot L^{-1}$ during the early Kungurian Stage [55] (Figure 7d). It means that an accelerated release of greenhouse gases may be responsible for the KICE. A large igneous

province (about 280 Ma) originated from a mantle plume that erupted in the north margin of Gondwana [56] in the early Kungurian. Lu et al. (2021) [21] considered that the Okhotsk Taigonos volcanic arc (278.8 ± 3. 0 Ma; [57]) and the Tarim LIP (284–272 Ma, with peak activity at ~280 Ma) are the important sources of CO_2 release in the early Kungurian. In addition, the volcanism caused by intense tectonic rifts under the influence of mantle plumes in the Shenza area of the Lhasa block [57–60] may also have provided additional greenhouse gases during the early Kungurian. A large amount of CO_2 entering water will affect the supply of carbon sources during the carbon isotope fractionation process, which could be a major cause of carbon isotope negative bias during KCIE.

After the KCIE in the middle Kungurian, the values of $\delta^{13}C_{carb}$ and $\delta^{13}C_{org}$ return to normal values, with a higher $\Delta^{13}C$ value of <29‰ (Figure 4). During the middle Kungurian, the volcanic activities and mantle plumes are not active [21]. The rapid chemical weathering of the volcanic rocks erupted during the early Kungurian reduces the concentration of CO_2 and cools the climate in the middle Kungurian. Meanwhile, the higher $\Delta^{13}C$ values may reflect enhanced primary productivity and photosynthesis. Therefore, the slightly positive or normal carbon isotopic compositions in the Kungurian represent an ameliorative environment during this time.

In the early Kungurian, the global climate changed from cold to warm [22]. Such warm climate conditions strengthened the occurrence of upwelling in low-latitude regions such as the Yangtze region in South China [29,61–63]. The low-latitude upwelling was expected to promote the algae blooms and higher primary productivity, which could increase the consumption of oxygen. Furthermore, the rapid transgression of sea level promoted the stratification of the water column, which is conducive to the preservation of organic-rich limestone during TST1. Kump and Arthur (1999) [64] suggested that increased global burial of organic matter could result in the removal of isotopically light carbon (^{12}C), leaving behind the heavier carbon isotope (^{13}C) in the marine carbon reservoir. This, in turn, would cause a rise in the $\delta^{13}C_{DIC}$ values of seawater, ultimately leading to more positive $\delta 13C_{carb}$ values in marine carbonate minerals. This may account for the increasing trend of $\delta^{13}C_{carb}$ values during the TST1 (Figures 4 and 7). As the temperature further rose, seawater stratification tended to be strengthened in association with the weakening of ocean currents, resulting in the formation of widely distributed organic-rich shales and siliceous rock during mfs1. The anoxic marine environment had a severely negative impact on the diversity of marine organisms. Foraminifera species numbers in the Gongchuan section of South China have dropped significantly (Figure 7f), and the conodont belt in the Tieqiao section has low abundance and low diversity [19]. The same decline situation occurs in relative species diversity in fusulinids of the North American shelf as well as eastern Australia and New Zealand (Figure 7g,h) [19,65–67].

In the middle Kungurian, the intensity of volcanic activity gradually weakened [55,56,68,69]. The climate turned toward cooling as the greenhouse gas input gradually decreased. Under such climatic conditions, the volume of oxygen-rich seawater increased due to enhanced ocean current circulation. During this process, the biodiversity, such as species of foraminifera, fusulinids, brachiopods, and bivalves, gradually recovered [19,65–67].

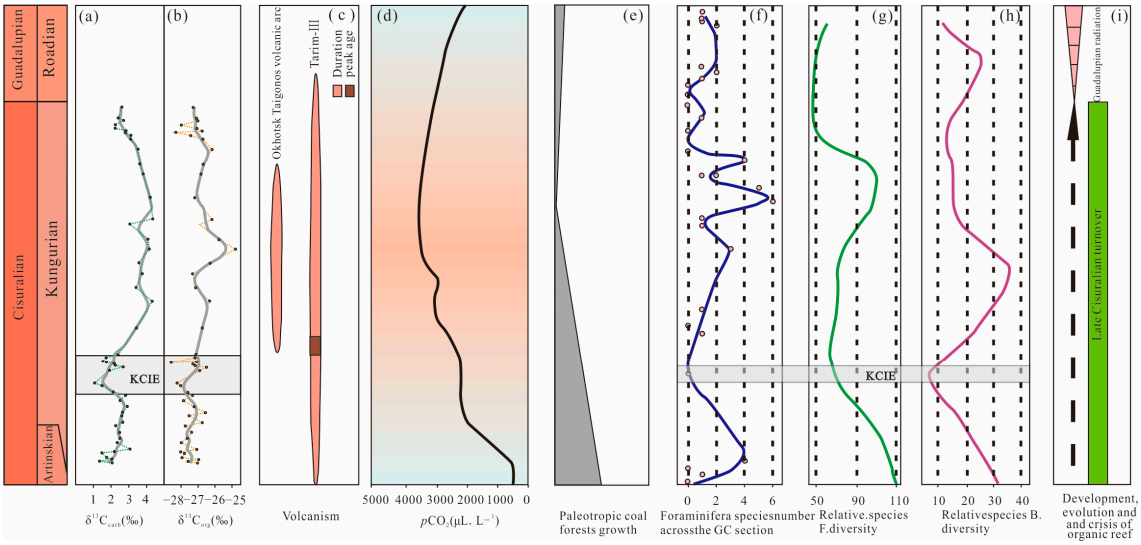


Figure 7. Correlations of organic carbon isotope and inorganic carbon isotope records and the paleoenvironmental events from the Permian-Kungurian stages. (**a**) Vertical change trends in $\delta^{13}C_{carb}$ in the study area (this study); (**b**) vertical change trends in $\delta^{13}C_{org}$ in the study area (this study); (**c**) volcanic activity from [56,57,68,69]; (**d**) carbon dioxide levels from [55]; (**e**) extent of paleotropical coal forests from [70]; (**f**) foraminifera species number across the GC section from [19]; (**g**) the relative species diversity in fusulinids of the North American shelf is taken from [65,66]; (**h**) the species diversity in brachiopods and bivalves of eastern Australia and New Zealand is adapted from [67]; (**i**) reef development, evolution, and crisis adapted from [71–73].

6. Conclusions

According to the Chihsia Formation of Putaoling section rock characteristics and the microscopic thin section authentication, seven types of facies are identified and are composed of lower slope, upper slope, and platform facies associations. The facies analyses show that the Kungurian Stage experiences two obvious transgressive-regressive cycles; paleoclimatic changes controlled the sedimentary records and sea level fluctuations. The Kungurian, corresponding to the maximum transgression of the Permian in South China, is the ice-melting beginning period of the LPIA.

Early Kungurian carbonate rock effectively recorded the presence of the short-lived KCIE. The rapid negative carbon isotope of the KCIE was closely related to the huge CO_2 emission, which entering seawater will affect the supply of carbon sources during the carbon isotope fractionation process. As the temperature increased, rising sea levels would accelerate the stratification of the water column, resulting in an anoxic environment. At this stage, lower oxygen content may cause a sharp decline in biological species such as foraminifera, fusulinids, brachiopods, and bivalves. In the middle Kungurian, the intensity of volcanic activity gradually weakened and the climate turned cold, which accelerated oceanic ventilation rates and led to increased oxygenation of deep-shelf water masses. Meanwhile, the higher $\Delta^{13}C$ values may reflect enhanced primary productivity and photosynthesis, which promote the prosperity of biological species. Our study provides a good case for better understanding the links between marine carbon cycle fluctuations and climate change.

Author Contributions: Conceptualization, C.F. and C.Z.; methodology, C.F. and X.B.; formal analysis, C.F. and C.Z.; investigation, C.Z., C.F., H.T. and J.C.; writing—original draft preparation, C.F. and C.Z.; supervision, H.W.; visualization, C.F. and H.W.; funding acquisition, C.F. All authors have read and agreed to the published version of the manuscript.

Funding: This work was supported by the Fundamental and Commonwealth Geological Survey of Oil and Gas in China (DD 20221662); the National Science Foundation of China (NSFC) (Nos. 42272118 and 41762003); the Open Fund of the Hubei Key Laboratory of Paleontology and Geological Environment Evolution (PEL-202206); the Geological Society of Jiangsu Province 2022 Key Academic Research Topics and Academic Exchange Direction Funding Project (DZXHP2022-05); and the Yunnan Province Science and Technology Department Project (No. 202101BA070001-145).

Data Availability Statement: The data presented in this study are available upon request from the corresponding author.

Conflicts of Interest: The authors declare no conflict of interest.

References

1. Smith, L.B., Jr.; Read, J.F. Rapid onset of late Paleozoic glaciation on Gondwana: Evidence from Upper Mississippian strata of the Midcontinent, United States. *Geology* **2000**, *28*, 279–282. [CrossRef]
2. Fielding, C.R.; Frank, T.D. Onset of the glacioeustatic signal recording late Palaeozoic Gondwanan ice growth: New data from palaeotropical East Fife, Scotland. *Palaeogeogr. Palaeoclimatol. Palaeoecol.* **2015**, *426*, 121–138. [CrossRef]
3. Tian, X.; Chen, J.; Yao, L.; Hu, K.; Qi, Y.; Wang, X. Glacio-eustasy and $\delta^{13}C$ across the Mississippian–Pennsylvanian boundary in the eastern Paleo-Tethys Ocean (South China): Implications for mid-Carboniferous major glaciation. *Geol. J.* **2020**, *55*, 2704–2716. [CrossRef]
4. Huang, S.; Shi, H.; Zhang, M.; Shen, L.; Liu, J.; Wu, W. Strontium Isotope Evolution and Global Sea-Level Changes of Carboniferous and Permian Marine Carbonate, Upper Yangtze Platform. *Acta Sedimentol. Sin.* **2013**, *19*, 481–487. (In Chinese with English abstract)
5. Laya, J.C.; Tucker, M.E.; Gröcke, D.R.; Perez-Huerta, A. Carbon, oxygen and strontium isotopic composition of low-latitude Permian carbonates (Venezuelan Andes): Climate proxies of tropical Pangea. *Geol. Soc. Lond. Spec. Publ.* **2013**, *376*, 367–385. [CrossRef]
6. Isbell, J.L.; Henry, L.C.; Gulbranson, E.L.; Limarino, C.O.; Fraiser, M.L.; Koch, Z.J.; Ciccioli, P.L.; Dineen, A.A. Glacial paradoxes during the late Paleozoic ice age: Evaluating the equilibrium line altitude as a control on glaciation. *Gondwana Res.* **2012**, *22*, 1–19. [CrossRef]
7. Montañez, I.P.; Poulsen, C.J. The Late Paleozoic Ice Age: An Evolving Paradigm. *Annu. Rev. Earth Planet. Sci.* **2013**, *41*, 629–656. [CrossRef]
8. Mii, H.; Grossman, E.L.; Yancey, T.E. Carboniferous isotope stratigraphies of North America: Implications for Carboniferous paleoceanography and Mississippian glaciation. *Geol. Soc. Am. Bull.* **1999**, *111*, 960–973. [CrossRef]
9. Bruckschen, P.; Oesmann, S.; Veizer, J. Isotope stratigraphy of the European Carboniferous: Proxy signals for ocean chemistry, climate and tectonics. *Chem. Geol.* **1999**, *161*, 127–163. [CrossRef]
10. Saltzman, M.R.; González, L.A.; Lohmann, K.C. Earliest Carboniferous cooling step triggered by the Antler orogeny? *Geology* **2000**, *28*, 347–350. [CrossRef]
11. Kametaka, M.; Nagai, H.; Zhu, S.; Takebe, M. Middle Permian Radiolarians from Anmenkou, Chaohu, Northeastern Yangtze platform, China. *Isl. Arc* **2009**, *18*, 108–125. [CrossRef]
12. Chen, J.; Montañez, I.P.; Qi, Y.; Shen, S.; Wang, X. Strontium and carbon isotopic evidence for decoupling of pCO_2 from continental weathering at the apex of the late Paleozoic glaciation. *Geology* **2018**, *46*, 395–398. [CrossRef]
13. Yao, L.; Aretz, M.; Chen, J.; Qi, Y. Earliest Carboniferous stromatolites from the Qianheishan Formation, Dashuigou section, northwestern China: Implications for microbial proliferation after the end-Devonian mass extinction. *Geol. J.* **2020**, *55*, 3361–3376. [CrossRef]
14. Yao, L.; Aretz, M.; Wignall, P.B.; Chen, J.; Vachard, D.; Qi, Y.; Shen, S.; Wang, X. The longest delay: Re-emergence of coral reef ecosystems after the Late Devonian extinctions. *Earth-Sci. Rev.* **2020**, *203*, 103060. [CrossRef]
15. Eyles, N. Earth's glacial record and its tectonic setting. *Earth-Sci. Rev.* **1993**, *35*, 1–248. [CrossRef]
16. Jones, A.T.; Fielding, C.R. Sedimentological record of the late Paleozoic glaciation in Queensland, Australia. *Geology* **2004**, *32*, 153–156. [CrossRef]
17. Isbell, J.L.; Miller, M.F.; Wolfe, K.L.; Lenaker, P.A. Timing of late Paleozoic glaciation in Gondwana: Was glaciation responsible for the development of Northern Hemisphere cyclothems? *Spec. Pap. Geol. Soc. Am.* **2003**, *370*, 5–24.
18. Liu, C.; Jarochowska, E.; Du, Y.; Vachard, D.; Munnecke, A. Microfacies and carbon isotope records of Mississippian carbonates from the isolated Bama Platform of Youjiang Basin, South China: Possible responses to climate-driven upwelling. *Palaeogeogr. Palaeoclimatol. Palaeoecol.* **2015**, *438*, 96–112. [CrossRef]
19. Liu, C.; Jarochowska, E.; Du, Y.; Munnecke, A.; Dai, X. Prevailing anoxia in the Kungurian (Permian) of South China: Possible response to divergent climate trends between the tropics and Gondwana. *Gondwana Res.* **2017**, *49*, 81–93. [CrossRef]
20. Liu, C.; Du, Y.; Jarochowska, E.; Yan, J.; Munnecke, A.; Lu, G. A major anomaly in the carbon cycle during the late Cisuralian (Permian): Timing, underlying triggers and implications. *Palaeogeogr. Palaeoclimatol. Palaeoecol.* **2018**, *491*, 112–122. [CrossRef]

21. Lu, J.; Zhou, K.; Yang, M.; Zhang, P.; Shao, L.; Hilton, J. Records of organic carbon isotopic composition ($\delta^{13}C_{org}$) and volcanism linked to changes in atmospheric pCO_2 and climate during the Late Paleozoic Icehouse. *Glob. Planet. Chang.* **2021**, *207*, 103654. [CrossRef]
22. Cheng, C.; Li, S.; Zhao, W.; Peng, L. The characteristics of microfacies and clay minerals of the Chihsia Formation carbonate rocks of Middle Permian in Susong, Anhui and its implication for sedimentary facies and paleoclimate. *Acta Geol. Sin.* **2016**, *90*, 1208–1219. (In Chinese with English abstract)
23. Chang, Y.; Dong, S.; Huang, D. On tectonics of "Poly-basement with one cover" in middle-lower Yangtze craton China. *Volcanol. Miner. Resour.* **1996**, *17*, 1–15. (In Chinese with English abstract)
24. Yin, H. South China defined as part of Tethyan archipelagic ocean system. *Earth Sci.-J. China Univ. Geosci.* **1999**, *24*, 1–12, (In Chinese with English abstract).
25. Yang, B. *Guadalupian Conodont Successions in Xuanhan, Sichuan and Chaohu, Anhui, South China and Their Correlation*; The University of Chinese Academy of Sciences: Beijing, China, 2015. (In Chinese with English abstract)
26. Jin, Y.; Shang, Q.; Wang, X. Permian stratigraphy of China. In *Biostratigraphy of China*; Zhang, W.T., Chen, P.J., Palmer, A.R., Eds.; Science Press: Beijing, China, 2003; pp. 331–378.
27. Yao, X.; Zhou, Y.; Hinnov, L.A. Astronomical forcing of a Middle Permian chert sequence in Chaohu, South China. *Earth Planet. Sci. Lett.* **2015**, *422*, 206–221. [CrossRef]
28. Shen, S.; Zhang, H.; Zhang, Y.; Yuan, D.; Chen, B.; He, W.; Mu, L.; Lin, W.; Wang, W.; Chen, J. Permian integrative stratigraphy and timescale of China. *Sci. China Earth Sci.* **2019**, *62*, 154–188. [CrossRef]
29. Wei, H.; Chen, D.; Wang, J.; Yu, H.; Tucker, M.E. Organic accumulation in the lower Chihsia Formation (Middle Permian) of South China: Constraints from pyrite morphology and multiple geochemical proxies. *Palaeogeogr. Palaeoclimatol. Palaeoecol.* **2012**, *353*, 73–86. [CrossRef]
30. Wilson, J.L. The Stratigraphy of Carbonate Deposits. In *Carbonate Facies in Geologic History*; Springer Study Edition; Springer: New York, NY, USA, 1975.
31. Randazzo, V.; Le Goff, J.; Di Stefano, P.; Reijmer, J.; Todaro, S.; Cacciatore, M.S. Carbonate slope re-sedimentation in a tectonically-active setting (Western Sicily Cretaceous Escarpment, Italy). *Sedimentology* **2020**, *67*, 2360–2391. [CrossRef]
32. Huang, H.; He, D.; Li, Y.; Wang, B. The prototype and its evolution of the Sichuan sedimentary basin and adjacent areas during Liangshan and Qixia stages in Permian. *Acta Petrol. Sin.* **2017**, *33*, 1317–1337. (In Chinese with English abstract)
33. Wang, Y.; Wen, Y.; Hong, H.; Xia, M.; Fan, Y.; Wen, L.; Kong, L.; Wu, C. Carbonate slope facies sedimentary characteristics of the Late Permian to Early Triassic in northern Sichuan Basin. *J. Palaeogeogr.* **2009**, *11*, 143–156. (In Chinese with English abstract)
34. Shen, C.; Tan, X.; Li, L.; Shi, K.; Su, C.; Lian, C.; Li, H.; Xiao, D. Sedimentary characters of carbonate platform marginal slope of the Early Cambrian in northern Sichuan Basin and perspective of deformation structure. *J. Palaeogeogr.* **2015**, *17*, 321–334. (In Chinese with English abstract)
35. Ross, C.A.; Ross, J.R.P. Late Paleozoic transgressive–regressive deposition. In *Sea-Level Changes—An Integrated Approach*; Wilgus, C.K., Hastings, B.S., Kendall, C.G.S.C., Posamentier, H.W., Ross, C.A., Van Wagoner, J.C., Eds.; SEPM Special Publications; Society of Economic Paleontologists, Mineralogists: Tulsa, OK, USA, 1988; Volume 42, pp. 227–247.
36. Embry, A.F. Transgressive–Regressive (T–R) Sequence Stratigraphy. In Proceedings of the 22nd Annual Gulf Coast Section SEPM Foundation Bob F. Perkins Research Conference, Houston, TX, USA, 8–11 December 2002; pp. 151–172.
37. Peng, X.; Xu, J.; Fang, C.; Shen, S.; Zhang, C. Sequence stratigraphic characteristics and shale gas exploration prospect of Middle Permian Qixia Formation in the Xuancheng Guangde Basin. *East China Geol.* **2022**, *43*, 154–166.
38. Vail, P.R. Seismic stratigraphy interpretation using sequence stratigraphy: Part 1: Seismic stratigraphy interpretation procedure. *AAPG Spec. Vol.* **1987**, *27*, 1–10.
39. Qiu, Z.; Wang, Q.; Zou, C.; Yan, D.; Wei, H. Transgressive–regressive sequences on the slope of an isolated carbonate platform (Middle–Late Permian, Laibin, South China). *Facies* **2014**, *60*, 327–345. [CrossRef]
40. Korte, C.; Kozur, H.W.; Veizer, J. $\delta^{13}C$ and $\delta^{18}O$ values of Triassic brachiopods and carbonate rocks as proxies for coeval seawater and palaeotemperature. *Palaeogeogr. Palaeoclimatol. Palaeoecol.* **2005**, *226*, 287–306. [CrossRef]
41. Wynn, T.C.; Read, J.F. Carbon–oxygen isotope signal of Mississippian slope carbonates, Appalachians, USA: A complex response to climate-driven fourth-order glacio-eustasy. *Palaeogeogr. Palaeoclimatol. Palaeoecol.* **2007**, *256*, 254–272. [CrossRef]
42. Kaufman, A.J.; Knoll, A.H. Neoproterozoic variations in the C-isotopic composition of seawater: Stratigraphic and biogeochemical implications. *Precambrian Res.* **1995**, *73*, 27–49. [CrossRef]
43. Wang, D.; Feng, X. Research on carbon and oxygen geochemistry of Lower Paleozoic in North China. *Acta Geol. Sin.* **2002**, *76*, 400–408. (In Chinese with English abstract)
44. Lehmann, M.F.; Bernasconi, S.M.; Barbieri, A.; McKenzie, J.A. Preservation of organic matter and alteration of its carbon and nitrogen isotope composition during simulated and in situ early sedimentary diagenesis. *Geochim. Cosmochim. Acta* **2002**, *66*, 3573–3584. [CrossRef]
45. Marais, D.J.D.; Strauss, H.; Summons, R.E.; Hayes, J. Carbon isotope evidence for the stepwise oxidation of the Proterozoic environment. *Nature* **1992**, *359*, 605–609. [CrossRef] [PubMed]
46. Li, P.; Wu, X.; Bai, X.; Yan, J.; Wang, H.; Huang, J. Sediment carbon pool and organic carbon burial in the Permian Qixia Formation at Shangsi Section in Guangyuan, Sichuan Province. *J. Palaeogeogr.* **2010**, *12*, 301–306. (In Chinese with English abstract)

47. Birgenheier, L.P.; Frank, T.D.; Fielding, C.R.; Rygel, M.C. Coupled carbon isotopic and sedimentological records from the Permian system of eastern Australia reveal the response of atmospheric carbon dioxide to glacial growth and decay during the late Palaeozoic Ice Age. *Palaeogeogr. Palaeoclimatol. Palaeoecol.* **2010**, *286*, 178–193. [CrossRef]
48. Van de Wetering, N.; Esterle, J.S.; Golding, S.D.; Rodrigues, S.; Götz, A.E. Carbon isotopic evidence for rapid methane clathrate release recorded in coals at the terminus of the Late Palaeozoic Ice Age. *Sci. Rep.* **2019**, *9*, 16544. [CrossRef]
49. Tierney, K.E. *Carbon and Strontium Isotope Stratigraphy of the Permian from Nevada and China: Implications from an Icehouse to Greenhouse Transition*; The Ohio State University: Columbus, OH, USA, 2010.
50. Frank, D.; Reichstein, M.; Bahn, M.; Thonicke, K.; Frank, D.; Mahecha, M.D.; Smith, P.; Van der Velde, M.; Vicca, S.; Babst, F. Effects of climate extremes on the terrestrial carbon cycle: Concepts, processes and potential future impacts. *Glob. Chang. Biol.* **2015**, *21*, 2861–2880. [CrossRef]
51. Fielding, C.R.; Frank, T.D.; Isbell, J.L. The late Paleozoic ice age—A review of current understanding and synthesis of global climate patterns, Resolving the late Paleozoic ice age in time and space. *Geol. Soc. Am. Spec. Pap.* **2008**, *441*, 343–354.
52. Chen, B.; Joachimski, M.M.; Shen, S.; Lambert, L.L.; Lai, X.; Wang, X.; Chen, J.; Yuan, D. Permian ice volume and palaeoclimate history: Oxygen isotope proxies revisited. *Gondwana Res.* **2013**, *24*, 77–89. [CrossRef]
53. Wang, Y.; Wang, J.; Chen, J.; Wang, W.; Shen, S.; Henderson, C.M. Progress, problems and prospects on the stratigraphy and correlation of the Kungurian Stage, Early Permian (Cisuralian) Series. *Acta Geol. Sin.-Engl. Ed.* **2011**, *85*, 387–398. [CrossRef]
54. Jin, Y.; Wang, X.; Shang, Q.; Wang, Y.; Sheng, J. Chronostratigraphic subdivision and correlation of the Permian in China. *Acta Geol. Sin.* **1999**, *2*, 97–108. (In Chinese with English abstract)
55. Saunders, A.; Reichow, M. The Siberian Traps and the End-Permian mass extinction: A critical review. *Chin. Sci. Bull.* **2009**, *54*, 20–37. [CrossRef]
56. Zhang, Y.; Zhang, K. Early Permian Qiangtang flood basalts, northern Tibet, China: A mantle plume that disintegrated northern Gondwana? *Gondwana Res.* **2017**, *44*, 96–108. [CrossRef]
57. Biakov, A. Permian biospheric events in Northeast Asia. *Stratigr. Geol. Correl.* **2012**, *20*, 199–210. [CrossRef]
58. Dickens, G.R.; O'Neil, J.R.; Rea, D.K.; Owen, R.M. Dissociation of oceanic methane hydrate as a cause of the carbon isotope excursion at the end of the Paleocene. *Paleoceanography* **1995**, *10*, 965–971. [CrossRef]
59. Hesselbo, S.P.; Gröcke, D.R.; Jenkyns, H.C.; Bjerrum, C.J.; Farrimond, P.; Morgans Bell, H.S.; Green, O.R. Massive dissociation of gas hydrate during a Jurassic oceanic anoxic event. *Nature* **2000**, *406*, 392–395. [CrossRef] [PubMed]
60. Jiang, G.; Kennedy, M.J.; Christie-Blick, N. Stable isotopic evidence for methane seeps in Neoproterozoic postglacial cap carbonates. *Nature* **2003**, *426*, 822–826. [CrossRef] [PubMed]
61. Wei, H.; Wang, J.; Yu, H.; Huang, B. Role of sea level fluctuation on the formation of organic carbon-rich sediments in the Chihsian formation in Sangzhi Area, western Hunan province. *Earth Sci.-J. China Univ. Geosci.* **2013**, *38*, 266–276. (In Chinese with English abstract)
62. Yan, J.; Zhao, K. Palaeogeography, palaeoclimate and palaeooceanic evolution in the Permian-Triassic East Tethys region coupled with multi-layer events on the surface of the Earth. *Sci. China Ser. D Earth Sci.* **2002**, *32*, 751–759. (In Chinese with English abstract)
63. Liu, X.; Yan, J.; Xue, W.; Ma, Z.; Li, B. Geobiological processes of Marine source rocks in the Middle Permian Qixia Formation, South China. *Sci. China Earth Sci.* **2014**, *44*, 1185–1192. (In Chinese with English abstract)
64. Kump, L.R.; Arthur, M.A. Interpreting carbon-isotope excursions: Carbonates and organic matter. *Chem. Geol.* **1999**, *161*, 181–198. [CrossRef]
65. Davydov, V.I.; Biakov, A.S. Discovery of shallow-marine biofacies conodonts in a bioherm within the Carboniferous–Permian transition in the Omolon Massif, NE Russia near the North paleo-pole: Correlation with a warming spike in the southern hemisphere. *Gondwana Res.* **2015**, *28*, 888–897. [CrossRef]
66. Davydov, V.; Biakov, A.; Isbell, J.; Crowley, J.; Schmitz, M.; Vedernikov, I. Middle Permian U–Pb zircon ages of the "glacial" deposits of the Atkan Formation, Ayan-Yuryakh anticlinorium, Magadan province, NE Russia: Their significance for global climatic interpretations. *Gondwana Res.* **2016**, *38*, 74–85. [CrossRef]
67. Waterhouse, J.; Shi, G. Climatic implications from the sequential changes in diversity and biogeographic affinities for brachiopods and bivalves in the Permian of eastern Australia and New Zealand. *Gondwana Res.* **2013**, *24*, 139–147. [CrossRef]
68. Xu, Y.; Wei, X.; Luo, Z.; Liu, H.; Cao, J. The Early Permian Tarim Large Igneous Province: Main characteristics and a plume incubation model. *Lithos* **2014**, *204*, 20–35. [CrossRef]
69. Sato, A.M.; Llambías, E.J.; Basei, M.A.S.; Castro, C.E. Three stages in the Late Paleozoic to Triassic magmatism of southwestern Gondwana, and the relationships with the volcanogenic events in coeval basins. *J. S. Am. Earth Sci.* **2015**, *63*, 48–69. [CrossRef]
70. Cleal, C.J.; Thomas, B.A. Palaeozoic tropical rainforests and their effect on global climates: Is the past the key to the present? *Geobiology* **2005**, *3*, 13–31. [CrossRef]
71. Kiessling, W. Secular variations in the Phanerozoic reef ecosystem. *Soc. Sediment. Geol. Spec. Publ.* **2002**, *72*, 625–690.
72. Flügel, E.; Kiessling, W. Patterns of Phanerozoic reef crises. *Soc. Sediment. Geol. Spec. Publ.* **2002**, *72*, 691–734.
73. Weidlich, O. Middle and Late Permian reefs—Distributional patterns and reservoir potential. *Soc. Sediment. Geol. Spec. Publ.* **2002**, *72*, 339–390.

Disclaimer/Publisher's Note: The statements, opinions and data contained in all publications are solely those of the individual author(s) and contributor(s) and not of MDPI and/or the editor(s). MDPI and/or the editor(s) disclaim responsibility for any injury to people or property resulting from any ideas, methods, instructions or products referred to in the content.